Quantitative research and correction of incident angle effect for wide-swath SAR images

LANG Wenhui[1], MO Ling[1], YANG Xuezhi[1], ZHANG Jie[2], MENG Junmin[2]

1. *School of Computer and Information, Hefei University of Technology, Hefei* 230009, *China*;
2. *The First Institute of Oceanography, SOA, Qingdao* 266061, *China*

Abstract: Based on a quantitative study of the incident angle effect of a wide-swath synthetic aperture radar (SAR) image, this paper proposes a class-based correction method for such an effect. The method achieves sampling by using watershed segmentation and regional labeling technology as well as a class-based radiation correction of land-cover backscatter values based on the cosine Lambert's law estimated through linear regression. Experimental results of the Envisat Advanced SAR (C-band horizontal-transmitting, horizontal-receiving polarization) data show that an incident angle effect is exerted on radar backscatter; the higher the moisture content of the land-cover type is, the more obvious the incident angle effect is. The correction of incident angle effect with this proposed algorithm is better than order cosine correction.

Key words: incident angle effect, watershed, quantitative study, Lambert's cosine law, linear regression

CLC number: TP751.1 **Document code:** A

Citation format: Lang W H, Mo L, Yang X Z, Zhang J and Meng J M. 2013. Quantitative research and correction of incident angle effect for wide-swath SAR images. Journal of Remote Sensing, 17(5): 1281-1294 [DOI: 10.11834/jrs.20132291]

1 INTRODUCTION

The backscatter coefficient of Synthetic Aperture Radar (SAR) depends on the characteristics of the feature (e.g., surface, roughness, structure, and water content) and on the interference of imaging system properties (e.g., incident angle, frequency, p olarization mode, and speckle noise) (Baker, et al., 1994; Yu, 2006). This coefficient is also influenced by environmental factors such as season. However, for the specific imaging platform and environment, non-stationary SAR images primarily depend on two factors: coherent spot noise and incident angle effect. Most studies have taken an interest in coherent spot noise. However, for both spaceborne and airborne wide-swath SAR, the incident angle effect has a severe impact on the accuracy of automatic interpretation; this effect is exerted not only on moderate-distance or remote-distance interpretation, but also on close interpretation and artificial interpretation (Leclerc, et al., 2001).

For distributed targets, the incident angle effect refers to r adar returns that are stronger in the close range and weaken as they move toward the far range. For example, for a Sahelian grassland image acquired by the Envisat Advanced SAR (Envisat ASAR) at C-band horizontal-transmitting, horizontal-receiving polarization with the incident angle changed from 15° to 45°, the corresponding backscatter variation is approximately -0.36 dB/° (Monsiváis, et al., 2006). For airborne SAR data, incident angle variation often achieves more than 40° (Menges, et al., 2001a). If the image acquired of the same region is observed with different geometric angles, the incident angle effect will be more significant (Menges, et al., 2001a). Ulaby (1975, 1978) and Makynen, et al. (2002) suggested that the incident angle effect d epends not only on the incident angle, but also on the roughness of the land cover, water content, and physical structure. However, almost all of the research and applications that considered incident angle variation have mainly been c ompleted on the image level with three categories. The most simplistic method is to ignore the part of the image where the i ncident angle is too large and its effect is strong, namely, the far range. This method has been applied mainly on airborne radar images (Rignot, et al., 1994; Israelsson, et al., 1994). An approach based on radar statistics along the range can be used to standardize angle dependence. In this empirical method, after the relationship between the radar backscatter and incident angle is found in a specific image, we use linear or second-order regression to normalize the observed backscatter values along the range in the incident angle extent. This method can be applied to the whole image and to the particular land-cover type in the image through a layer mask, such as the correction of the incident angle effect of the airborne radar (Menges, et al., 2001b). The limitation of this correction method is that it depends on a specific radar dataset and cannot be replicated in other images. Another application with a statistical method based on surface fitting

Received: 2012-10-25; **Accepted:** 2013-01-31; **Version of record first published:** 2013-02-07

Foundation: National Natural Science Foundation of China (No. 61271381, 41076120, 60890075), Basic Scientific Research Business Expenses Special Funding of Central University (No. 2012HGCX0001); Talent Development Grants of Anhui Province (No. 2008Z054), SRF for ROCS, SEM.

First author biography: LANG Wenhui (1965—), male, associate professor. His research interests are remote sensing image processing and intelligent information processing. E-mail: langwh@hfut.edu.cn

technology is the use of the parameter polynomial model fit for the whole image data, which considers information entropy as a criterion function (Lang, et al., 2011). However, this method is also global. The third method is to develop a simple physical model that explains specific angular dependence in terms of the incident angle (θ_i) as an independent variable. Based on the SAR image dominant land-cover type, the corresponding physical model is applied to the whole image correction. However, this method needs the dominant land-cover type of prior knowledge in the image and cannot compensate for the i ncident angle effect of the other land-cover type in the image (Leclerc, et al., 2001).

Therefore, according to the given research area based on the data of Envisat ASAR in a wide model, assuming that the same land-cover type has the same roughness, moisture content, and physical structure, the present study uses watershed segmentation and regional marker technology to realize land-cover sampling and then uses basic statistics to complete quantitative research on the angle effect at land-cover level. On this basis, the class-based standardization and radiation correction of land-cover backscatter are achieved based on the cosine Lambert's law estimated through linear regression.

2 RESEARCH AREA AND TEST DATA

The study site includes Bohai Sea, Shangdong Peninsula, Liaodong Peninsula, Littoral Plain, and part of the Yellow Sea (34°N—41°N, 115°E—124°E). This area is mainly composed of plains, power sand silt mass coasts, and offshores. The terrain is flat and straight shoreline.

Bohai Sea covers the Bohai Straits, Liaodong Bay, Bohai Bay, Laizhou Bay, and the central basin of the Bohai Sea. Given its location in the mid-latitude monsoon climate zone, which is swept by the Siberian cold wave, different degrees of freezing phenomena are observed in Bohai Sea every winter. The freezing period usually begins in December. The last glacial maximum is from January to February in the following year. The melting ice period is in February. The seven ASAR wide-swath mode (WSM) scenes used in the test with a swath width of 405 km at 150 m spatial resolution are distributed during this period. Fig. 1(a)—Fig. 1(c) show three of these scenes. The scene in Fig. 1(a), the range distance of which increases toward the west, was obtained on December 21, 2005. The scene is in the initial ice period, and landfast ice has formed at the beginning. Fig. 1(b) was acquired on February 6, 2006, during which the range distance increased toward the east. This period is the last glacial maximum. The ice outer line of Bohai Bay is up to 14 n miles, general ice thickness is between 5 cm and 10 cm, and the largest ice thickness is 25 cm. Fig. 1(c) was acquired on February 23, 2006, during which the range distance increased toward the west; it occurred in the ice melting period. An evident incident angle effect can be observed in these three images, hindering a sea ice analyst's interpretation of sea ice. Thus, we need to compensate for the incident angle effect. To ensure the precision of sampling, we also utilize the ice chart of the same period (Zhang, et al., 2006) and optical satellite imagery as auxiliary information.

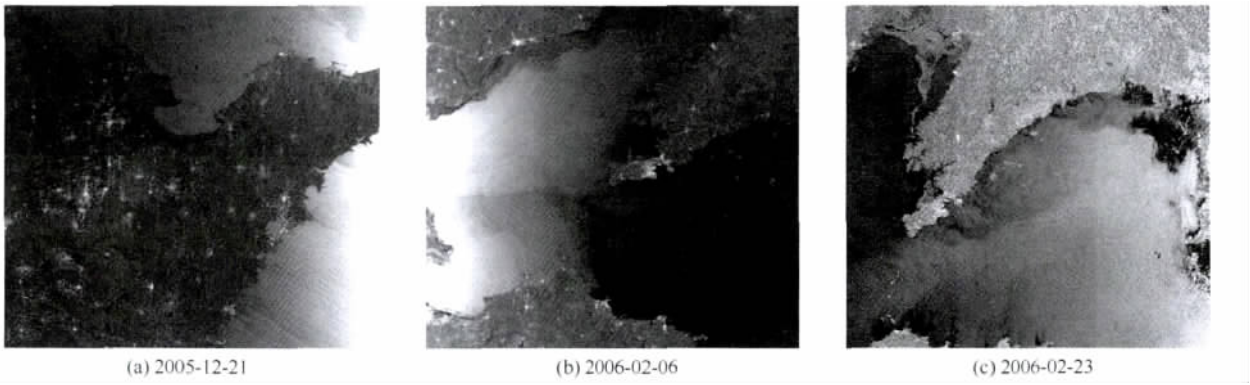

Fig. 1 Amplitude image of Bohai Bay

3 ABSOLUTE CALIBRATION

Although uncalibrated SAR imagery is sufficient for qualitative use, calibrated SAR images are essential to the quantitative use of SAR data (Johannessen, et al., 2007). ASAR WSM is a ground-range-detected product. ASAR ground-range images have all been applied to antenna gain pattern compensation (based on ellipsoid approximations) and range spreading loss correction during the formation of the images. Therefore, we do not consider the influence of the two in the following calibration process.

For ground-range-detected products, the general form of the SAR intensity image is shown as Eq. (1). The equation gives the effect of the local incident angle on the DN stored in a slant-range pixel without noise (Leclerc, et al., 2001)

$$\begin{aligned} DN^2(i,j) &= \frac{K\sigma^0(i,j)}{\sin[\theta_r(i,j)]\cos[\theta_a(i,j)]} \quad \theta_r,\theta_a < 90^\circ \\ DN^2(i,j) &= 0 \quad \theta_r \geqslant 90^\circ \end{aligned} \tag{1}$$

where K is the absolute calibration constant, $\sigma^0(i,j)$ is the backscatter coefficient for pixel (i,j), $DN^2(i,j)$ is the pixel intensity for pixel (i,j) (DN is proportional to backscatter amplitude), θ_r is the local incident angle in the range direction, and θ_a is the local incident angle in the azimuth direction. The right side of Eq. (1) indicates that the size of the scattering area in ground-range-detected products is the corresponding area in the slant range of $[\sin(\theta_r)\cos(\theta_a)]^{-1}$ times.

For WSM products at the reference elevation, assuming that the terrain is flat ($\theta_a = 0$), the sigma zero is defined as follows (Rosich & Meadows, 2004):

$$\sigma^0(i,j) = \frac{DN^2(i,j)}{K}\sin[\theta_i(i,j)] \quad (2)$$

where θ_i is the angle between radar sight and the horizontal plane perpendicular. When the area is flat, $\theta_i = \theta_r$. The K used in the test image is 7413102.5. The sine of the incident angle is used to compensate for the change in pixel size because the ratio of the slant distance projection resolution cell length and the corresponding length in the ground range is $\sin(\theta_r)$, which increases the backscatter $\sigma^0(i,j)$ with the incident angle. The compensation effect of the incident angle is shown in Fig. 8(a)—Fig. 8(c). With increasing distance, the three ASAR WSM images still have an incident angle effect after absolute calibration.

4 METHOD

4.1 Sampling

To facilitate the quantitative research and correction of the incident angle effect, this study designs a unique homogeneous backscattering region sampling method. Land-cover type is usually complex and confusing; the method based on space knowledge and homogeneous area intensity information is s ampling for land-cover type. Space knowledge is from the optical imagery in the same area and the ice chart of the same period; it provides information about land-cover type and analyzes initial sampling range for radar intensity. Therefore, the test image can be classified into three types: sea ice, open water, and land. Sea ice is mainly distributed in coastal areas, and the span has a narrow range distance even in the last glacial maximum. No waves in the open water are observed during the study period. The land part corresponds to the coastal zone of the Shangdong Peninsula, Liaodong Peninsula, and Littoral Plain. The study area is flat, and so the terrain and local incident angle effect can be ignored. Shadow and layer areas are masked out in the images by using the digital elevation model.

The land-cover type must be accurately extracted by s egmentation and classification techniques in image processing. Speckle noise is a major obstacle that affects the accuracy of the SAR image classification. Sampling based on intensity information should control the radar spots. The image is segmented with a watershed algorithm (Vincent & Soille, 1991) that d ivides the image into many small regions with relatively uniform backscatter in each. Suppose each region v consists of a set of sites $\boldsymbol{S}_v$ that belongs to it. The effect of the speckle noise is reduced because the feature vectors of the individual sites $\{\boldsymbol{y}_s \mid s \in \boldsymbol{S}_v\}$ can be averaged into one feature vector $\boldsymbol{y}_v$ for the entire region. K means clustering algorithm based on the number of land-cover types is adopted to find an optimal labeling of each watershed region. To ensure the gradient of the incident angle effect, the areas in this step are not merged. Segmentation and classification techniques in this paper refer to a non-supervised lower classification method.

The momon units of analysis for radar backscattering are the 1° range bins of incident angles. Each bin in the image stands for 1° of incident angle observation. After sampling for the land-cover type, the average sigma value is given by a range bin. The sigma value curve moving from near to far range of r elated land-cover type is also obtained. The entire sampling process is shown in Fig. 2.

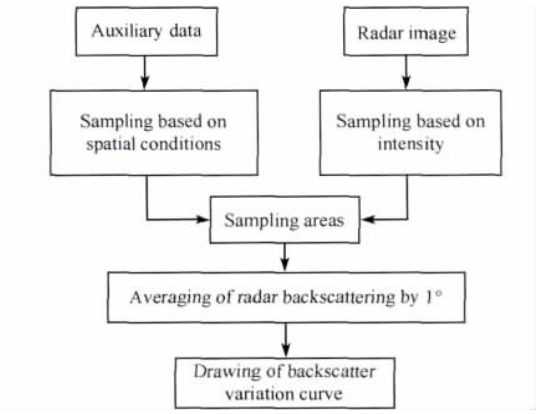

Fig. 2 Sampling process

In most studies, ground survey is usually the first choice of learning sample selection. However, for scenarios in which ground survey is limited or the accessibility of the areas is hampered by local conditions, such as in the Arctic, traditional ground survey is unrealistic. The proposed approach of spatial knowledge and homogenous area intensity information results in an efficient and optimal strategy that is worth using.

4.2 Radar backscattering analysis at land-cover level

For Envisat ASAR images, this section describes the quantitative research based on land-cover types that consider reflective targets and analyze the radar backscatter.

We adopt the sampling method described in Fig. 2 and identify the sea ice, open water, and land areas (white, light gray, and dark gray areas, respectively, in Fig. 3). The sigma zero trend is drawn after traditional absolute calibration. The sea ice of the

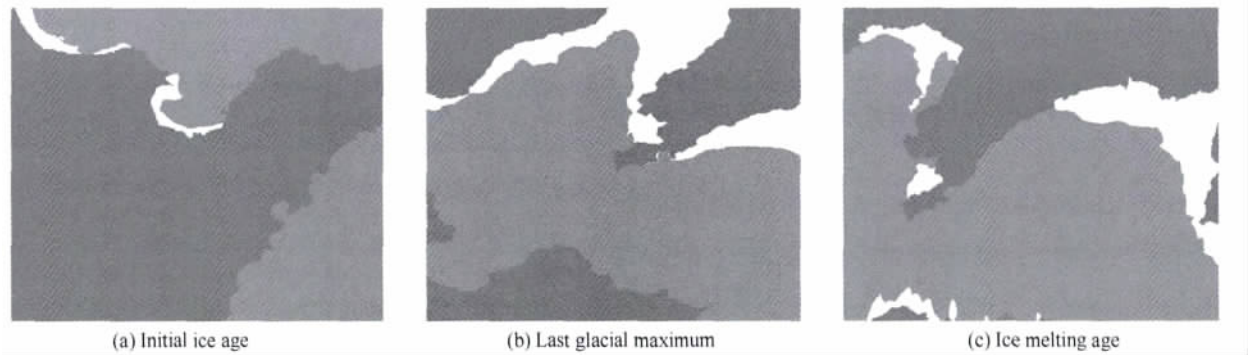

(a) Initial ice age (b) Last glacial maximum (c) Ice melting age

Fig. 3 Sampling images

three images is in the initial ice age, the last glacial maximum, and the melting age. The images in Fig. 4 show the obvious incident angle effect. The curve for the open water is the volatility maximum with respect to changes in sea ice and land. The same scattering trend along the range is observed in the land area of the three images.

Data analysis of sea ice indicates that sea ice, open water, and land have different backscatter variations with incident angle change after the absolute calibration, as shown in Table 1. The radiation variation of the open water is the most obvious. These changes are observed in the same land-cover type. The same land-cover type is assumed to have the same roughness, moisture content, and physical structure; therefore, the decrease of average sigma value is attributed only to the incident angle and the land-cover type. A method that considers correction at the land-cover level rather than of the whole image is warranted because backscatter variation with the incident angle does not equally affect all land-cover types.

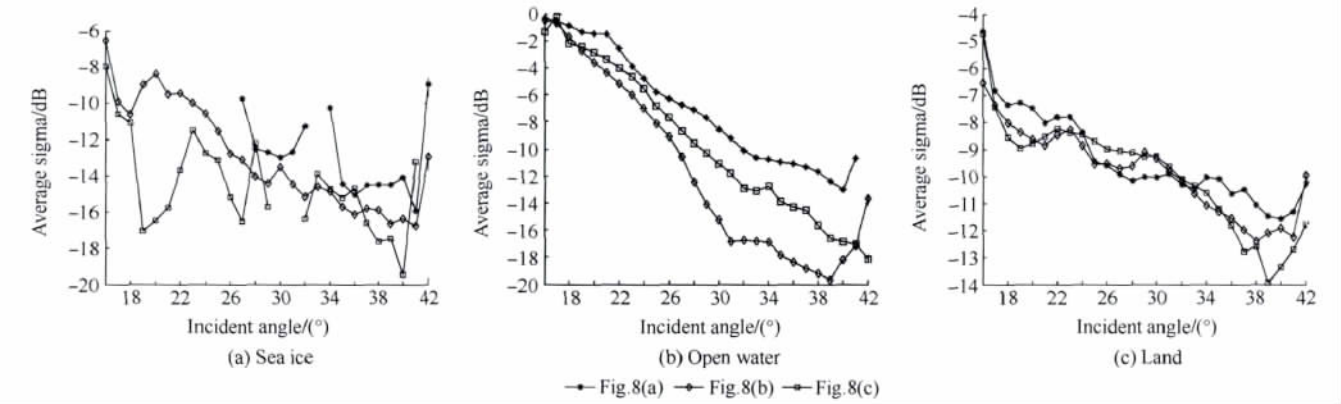

Fig. 4 Backscatter plot for land-cover types

Table 1 Backscattering coefficients of sea ice, open water, and land

Backscattering/dB	Sea ice			Open water			Land		
	Maximum	Minimum	Variation	Maximum	Minimum	Variation	Maximum	Minimum	Variation
Fig. 1(a)	-9.10	-16.11	7.01	-0.02	-13.20	13.18	-5.17	-11.76	6.59
Fig. 1(b)	-7.08	-16.93	9.85	-0.08	-19.86	19.78	-7.10	-12.43	5.39
Fig. 1(c)	-8.52	-19.64	11.12	-0.23	-18.14	17.91	-4.12	-13.92	9.80

4.3 Correction method

For the various classes of the study, a method to compensate for the effect is applied once the incident angle effect is quantified.

The calibration model based on the theory of radiative transfer/Lambert's law (Ulay, et al., 1981; Menges, et al., 2001b) is proposed in this paper. If the scattering target is a perfect L ambertian scattering cross section and the radiation wave front is reflected to the antenna completely backward, the scattering coefficient σ^0 obeys a simple cosine law

$$\sigma^0 = \sigma_0^0 \cos[\theta_r(i,j)] \cos[\theta_a(i,j)] \quad (3)$$

where σ_0^0 is independent of the coefficient of the land-cover types.

For a perfectly rough surface, the wave front is not totally reflected, and backscatter coefficients follow the square cosine law

$$\sigma^0 = \sigma_0^0 \cos^2[\theta_r(i,j)] \cos^2[\theta_a(i,j)] \quad (4)$$

If the scattering target is distributed by the independent point reflector.

$$\sigma^0 = \sigma_0^0 \quad (5)$$

A single model cannot be suitable for any land-cover presented in the image, and we want to find a generic backscatter model that is compatible with various land-cover types. Thus, a universal description is designed based on Eq. (3) —Eq. (5)

$$\sigma^0 = \sigma_0^0 \{\cos[\theta_r(i,j)] \cos[\theta_a(i,j)]\}^n \quad (6)$$

where n is not limited to 0, 1, 2. A better normalized curve can be produced by searching for a preferred estimate of n. Thus, better flatness degrees along the range distance are observed.

Assuming that the terrain is flat ($\theta_a = 0$) and $\theta_i = \theta_r$, Eq. (6) can be simplified to

$$\sigma^0 = \sigma_0^0 \cos^n(\theta_i) \quad (7)$$

To compensate for the incident angle effect, we estimate n by linear regression

$$y = nx + b \quad (8)$$

where $y = \lg(\sigma^0)$, $x = \lg(\cos\theta_i)$, $b = \lg(\sigma_0^0)$.

Therefore, the correction model is

$$\sigma_n^0 = \sigma^0 \cos^n(\theta_i) + b \quad (9)$$

5 EXPERIMENTAL RESULTS AND ANALYSIS

For the three Envisat ASAR images, the backscatter values are normalized for the three affected classes: sea ice, open water, and land. The coefficients n and b for these classes, estimated via a regression model (Eq. (8)) are shown in Table 2. We also model the backscatter of sea ice, open water, and land, and then correct the incident angle effect. Experiments are developed by the p roposed correction method, which is compared with class-based correction, absolute calibration, and first-order cosine cor-

rection (Fig. 5—Fig. 7) (Menges, et al., 2001a; Ulaby et al., 1981). The e xperiment results indicate that the method adopted in this paper is simple, easy to implement, and requires little time. The method can effectively correct the incident angle effect of Envisat ASAR images.

Table 2 Coefficients *n* and *b* for sea ice, open water, and land

Fig. 8	Sea ice		Open water		Land	
	n	*b*	*n*	*b*	*n*	*b*
(a)	0.81	-1.49	12.04	-0.11	1.85	-1.54
(b)	2.65	-1.75	10.17	-0.64	2.18	-1.36
(c)	1.54	-1.63	10.29	-0.45	2.58	-1.66

Fig. 5—Fig. 7 demonstrate that the brightness of sea ice, open water, and land in the range is enhanced by absolute calibration, first-order cosine correction, and class-based correction. However, absolute calibration and first-order cosine correction are applied in the whole image, ignoring the influence of the s patial distribution of the land-cover type. Although the incident angle effect is compensated for, the corrected images still have the incident angle effect in the far range.

This study uses a class method based on land-cover types. After the class-based correction, the backscatter values of sea ice, open water, and land obtain different compensations. We also o btain better results with relatively uniform backscatter and eliminate the incident angle effect in the far range. Overall, the curves of class-based correction are smoother than those of absolute calibration and first-order cosine correction, and the land-cover types in the image are more likely to be distinguished. Fig. 8 to Fig. 10 show that sea ice, open water, and land have a better visual result via class-based correction than via absolute calibration and first-order cosine correction. The incident angle effect is eliminated and mainly reflected only on open water in the far range, the backscattering of which is significantly enhanced. The gray values of sea ice, open water, and land are different, thereby facilitating artificial interpretation and improving senior classification accuracy.

For different land-cover types, backscatter values affected by the incident angle and the correction factor are usually different. Given that the incident angle effect on the land-cover type with higher moisture content (e. g., open water) is more noticeable than on sea ice and land, the correction factor of this type is larger. After correction, an obvious improvement is o bserved in the area of open water. Take sea ice for example. A lthough sea ice takes up only a small proportion in the whole scene, the incident angle effect can be appreciable. Table 2 reveals that the correction factor of sea ice in the last glacial maximum is the largest, whereas that in the initial ice age is the minimum.

For most of the classes, backscatter systematically decreases from close range to far range. This result contradicts several studies that suggest that after correcting for topographic effects, the incident angle effect can be ignored for spaceborne observations. The results of this study indicate that when dealing with spaceborne observations with a swath of several hundreds of k ilometers, the incident angle effect on radar backscatter should be considered.

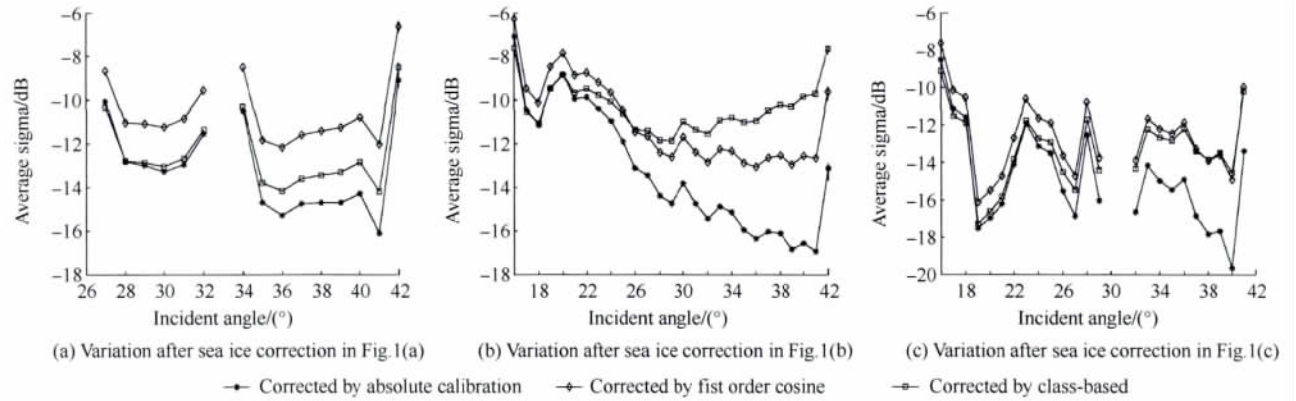

Fig.5 Curves of sea ice backscatter estimates with incident angle

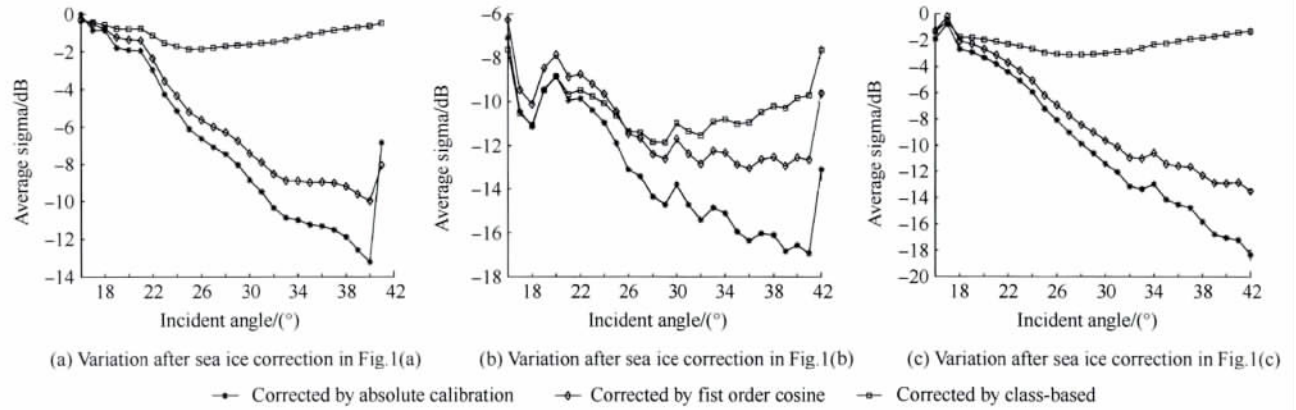

Fig.6 Curves of open water backscatter estimates with incident angle

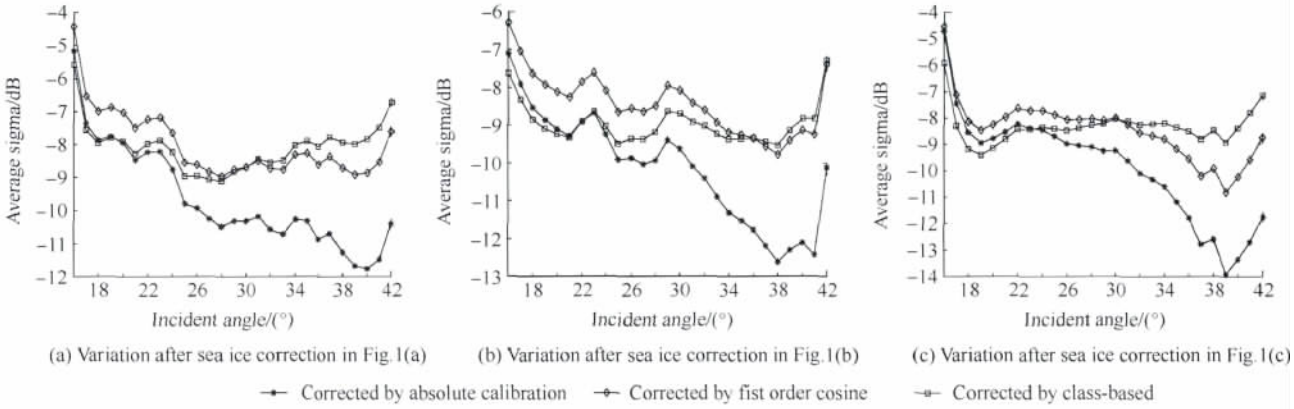

(a) Variation after sea ice correction in Fig.1(a) (b) Variation after sea ice correction in Fig.1(b) (c) Variation after sea ice correction in Fig.1(c)

Fig.7 Curves of land backscatter estimates with incident angle

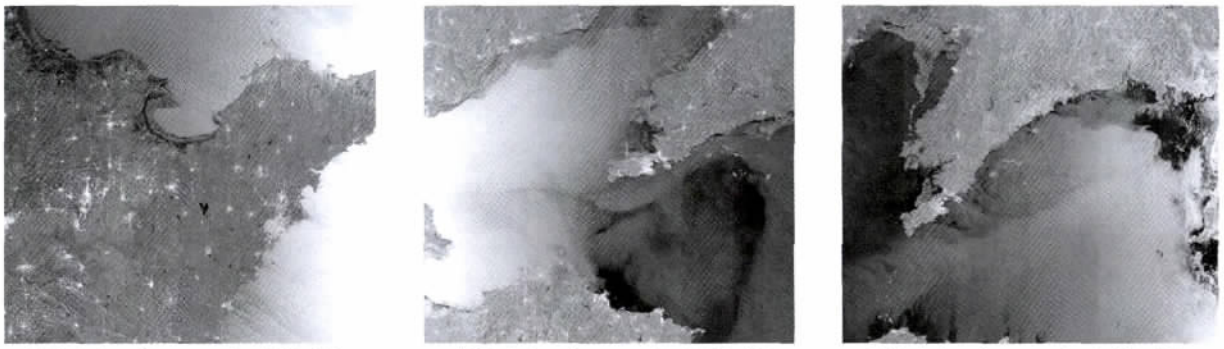

(a) Variation after correction in Fig.1(a) (b) Variation after correction in Fig.1(b) (c) Variation after correction in Fig.1(c)

Fig.8 Bohai Bay ASAR images after absolute calibration

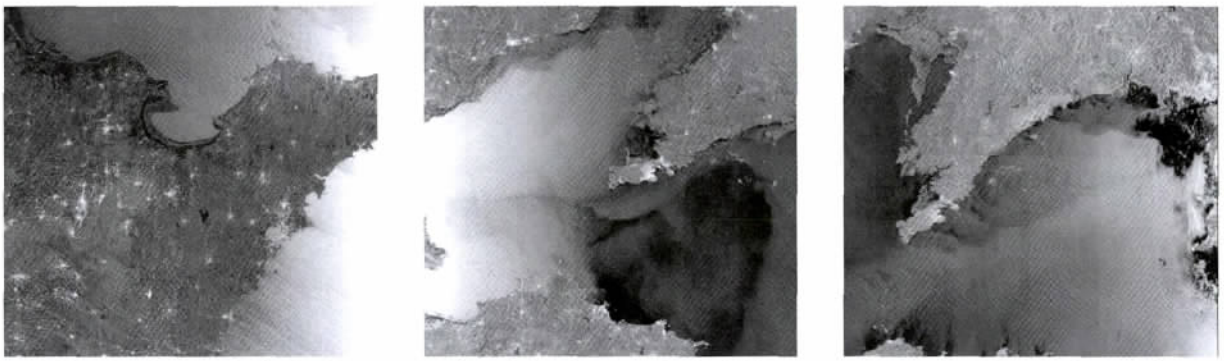

(a) Variation after correction in Fig.8(a) (b) Variation after correction in Fig.8(b) (c) Variation after correction in Fig.8(c)

Fig.9 Bohai Bay ASAR images after first-order cosine correction

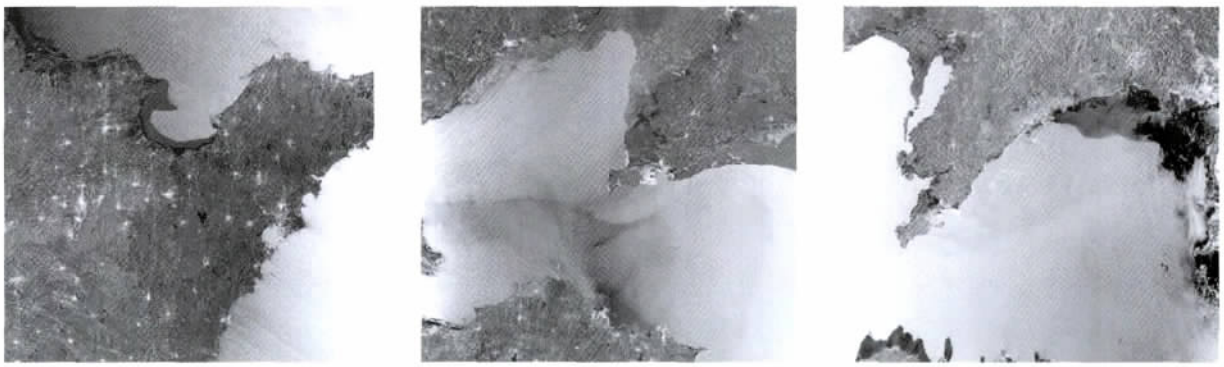

(a) Variation after correction in Fig.8(a) (b) Variation after correction in Fig.8(b) (c) Variation after correction in Fig.8(c)

Fig.10 Bohai Bay ASAR images after class-based correction

6 CONCLUSION

The angle change of backscatter is measured and analyzed for several ASAR WSM images, which confirms that the incident angle effect in the mode of wide observation width cannot be neglected, particularly on sea ice and open water. Based on quantitative research, radiation correction in land-cover backscatter values based on the cosine Lambert's law estimated through linear regression is performed. Compared with the traditional effect that uses the absolute calibration formula, the method in this paper can efficiently compensate for the incident angle effect of wide observation width SAR images.

Most satellite ground receiving stations offset the backscatter change in the range direction by using the sine part in the absolute calibration or the first-order cosine correction. Thus, changes in land-cover types have been ignored. For the application of wide observation width satellite SAR, however, a more thorough correction scheme should be considered, namely, the scheme regarding the distribution of land-cover types. The estimated values of n and b in the correction result can also be used for the senior classification of land-cover types.

REFERENCES

Baker J R, Mitchell P L, Cordey R A, Groom G B, Settle J J and Stileman M R. 1994. Relationships between physical characteristics and polarimetric radar backscatter for corsican pine stands in thetford forest, U. K. International Journal of Remote Sensing, 15(14): 2827 – 2849 [DOI: 10.1080/01431169408954287]

Israelsson H, Askne J and Sylvander R. 1994. Potential of SAR for forest bole volume estimation. International Journal of Remote Sensing, 15(14): 2809 – 2826 [DOI: 10.1080/01431169408954286]

Johannessen O M, Alexandrov V Y, Frolov I Y, Sandven S, Pettersson L H, Bobylev L P, Kloster K, Smirnov V G, Mironov Y U and Babich N G. 2007. Remote Sensing of Sea ice in the Northern Sea Route: Studies and Applications. Chichester, UK: Springer

Kanungo T, Mount D M, Netanyahu N S, Piatko C D, Silverman R and Wu A Y. 2002. An efficient K-means clustering algorithm: analysis and implementation. IEEE Transactions on Pattern Analysis and Machine Intelligence, 24(7): 881 – 892 [DOI: 10.1109/TPAMI.2002.1017616]

Lang W H, Wang J S, Yang X Z and Wang G Z. 2011. Multi-exponential model based bias field correction of SAR sea ice image. Journal of Remote Sensing, 15(1): 163 – 172

Leclerc G, Beaulieu N and Bonn F. 2001. A simple method to account for topography in the radiometric correction of radar imagery. International Journal of Remote Sensing, 22(17): 3553 – 3570 [DOI: 10.1080/01431160010007060]

Mäkynen M P, Manninen A T, Similä M H, Karvonen A J and Hallikainen M T. 2002. Incidence angle dependence of the statistical properties of C-Band HH-Polarization backscattering signatures of the Baltic sea ice. IEEE Transactions on Geoscience and Remote Sensing, 40(12): 2593 – 2605 [DOI: 10.1109/TGRS.2002.806991]

Menges C H, Van Zyl J J, Hill G J E and Ahmad W. 2001a. A procedure for the correction of the effect of variation in incidence angle on AIRSAR data. International Journal of Remote Sensing, 22(5): 829 – 841

Menges C H, Hill G J E, Ahmad W and van Zyl J J. 2001b. Incidence angle correction of AirSAR data to facilitate land-cover classification. Photogrammetric Engineering and Remote Sensing, 67(4): 479 – 489

Monsiváis A, Chenerie I, Baup F, Mougin E and Sarabandi K. 2006. Angular normalization of ENVISAT ASAR data over Sahelian-grassland using a coherent scattering model. Progress in Electromagnetics Research Symposium, 2(1): 94 – 98

Oliver C and Quegan S. 2004. Understanding Synthetic Aperture Radar Images. Raleigh, NC: SciTech Publishing, p197

Rignot E, Way J, Williams C and Viereck L, 1994. Radar estimates of a bove ground biomass in boreal forests of interior Alaska. IEEE Transactions on Geoscience and Remote Sensing, 32(5): 1117 – 1124 [DOI: 10.1109/36.312903]

Rosich B and Meadows P. 2004. Absolute calibration of ASAR Level 1 products generated with PF-ASAR. Issue 1, Revision 5, European Space Agency

Ulaby, F T, Batlivala P P and Dobson M C. 1978. Microwave backscatter dependence on surface roughness, soil moisture, and soil texture: Part I. Bare soil. IEEE Transactions on Geoscience Electronics, GE – 16(1978) 4: 286 – 295

Ulaby F T, Bush T F and Batlivala P P. 1975. Batlivala, Radar response tovegetation II: 8—18 GHz band. IEEE Transactions on Antennas and Propagation, AP – 23(1975) 5: 608 – 618

Ulaby F T, Moore R K and Fung A K. 1981. Microwave Remote Sensing: Active and Passive: Vol. I microwave remote sensing fundamentals and radiometry Vol. II radar remote sensing and surface scattering and emission theory Vol. III from theory to applications. Addison-Wesley, 456

Vincent L and Soille P. 1991. Watersheds in digital spaces: an efficient algorithm based on immersion simulations. IEEE Transactions on Pattern Analysis and Machine Intelligence, 13(6): 583 – 598 [DOI: 10.1109/34.87344]

Yu Q Y. 2006. Automated SAR Sea Ice Interpretation. Canada: University of Waterloo

Zhang Q W, Bai S, Li B H, Liu Y and Li C H. 2006. Sea ice condition and ice warning in the Bohai sea during the 2005—2006 winter. Marine Forecasts, 23(supplement): 17 – 26

宽观测带 SAR 图像入射角效应量化研究与校正

郎文辉[1]，磨玲[1]，杨学志[1]，张杰[2]，孟俊敏[2]

1. 合肥工业大学 计算机与信息学院，安徽 合肥 230009;
2. 国家海洋局 第一海洋研究所，山东 青岛 266061

摘 要: 针对宽观测带 SAR 图像,在对入射角效应量化研究的基础上,提出了一种入射角效应按类校正方法。利用分水岭分割和区域标记技术实现地物取样,基于结合线性回归估计的余弦朗伯定律,实现对地物后向散射值的按类辐射校正。针对 Envisat ASAR C 波段 HH 极化数据的实验结果表明,入射角效应对雷达后向散射有明显的影响,含水量越高的地物类型,入射角效应越明显。利用本文方法进行入射角效应校正的效果优于绝对定标和一阶余弦校正的效果。

关键词: 入射角效应,分水岭,量化研究,余弦朗伯定律,线性回归

中图分类号: TP751.1 **文献标志码**: A

引用格式: 郎文辉,磨玲,杨学志,张杰,孟俊敏. 2013. 宽观测带 SAR 图像入射角效应量化研究与校正. 遥感学报,17(5): 1281 – 1294

Lang W H, Mo L, Yang X Z, Zhang J and Meng J M. 2013. Quantitative research and correction of incident angle effect for wide-swath SAR images. Journal of Remote Sensing, 17(5): 1281 – 1294 [DOI: 10.11834/jrs.20132291]

1 引 言

SAR 后向散射系数一方面取决于地物的自身特性(表面粗糙度、体结构和含水量等),另一方面还依赖于成像系统特性(入射角、频率、极化模式和相干斑噪声等),此外还受到环境因素(如季节)的干扰(Baker 等,1994; Yu,2006)。然而,针对特定的成像平台和环境,SAR 图像的非平稳性主要取决于两个因素: 相干斑噪声和入射角效应。虽然学术研究的重点大多集中于前者,但对星载宽观测带(如 ScanSAR)和机载 SAR 图像而言,入射角效应的存在,不仅影响中、远距自动解译的精度,有时对近距的自动解译也有非常严重的影响,甚至影响人工判读的效果(Leclerc 等,2001)。

对分布式目标而言,入射角效应是指雷达回波在近距较强,随着向远距移动将逐渐减弱。例如,一幅由环境卫星先进合成孔径雷达(ENVISAT ASAR)在 C 波段 HH 极化采集的萨赫勒草地图像,入射角范围在 15°到 45°,对应的后向散射变化大约为 – 0.36 dB/1°(Monsiváis 等,2006);而对机载 SAR 数据来说,入射角的变化往往能达到 40°以上(Menges 等,2001a);如果考虑利用从不同几何视角对同一地区观测采集的图像,则入射角效应的影响更为显著(Menges 等,2001a)。Ulaby 等人(1975,1978)和 Mäkynen 等人(2002)的研究进一步表明,入射角效应不仅取决于入射角,而且取决于地物的粗糙度、含水量和物理结构。然而,现有考虑入射角变化的几乎所有研究和应用都是在图像水平上完成的,主要分为 3 类。其中最简单的方法是忽略入射角过大且影响非常剧烈的图像部分,即远距部分。该方法主要应用在机载雷达图像中(Rignot 等,1994; Israelsson 等,1994)。基于雷达统计量的方法可用于对入射角依赖性进行规格化。在这种经验方法中,针对指定图像找出雷达后向散射和入射角间的关系后,利用线性或二阶回归,沿距离向在入射角范围内对被观测散射值进行规格化。这种方法可应用到图像的整个区域,也可利用分层面罩实现对图像中出现的特定地物类型的校正,如对机载

收稿日期: 2012-10-25; 修订日期: 2013-01-31; 优先数字出版日期: 2013-02-07

基金项目: 国家自然科学基金(编号: 61271381,41076120,60890075);中央高校基本科研业务费专项资金(编号: 2012HGCX0001);安徽省人才开发基金(编号: 2008Z054);教育部留学回国人员科研启动基金资助项目

第一作者简介: 郎文辉(1965—),男,博士,副教授。主要研究领域是遥感图像处理及智能信息处理。E-mail: langwh@hfut.edu.cn

雷达图像中入射角影响的校正(Menges 等,2001b),这种校正方法的缺点是它依赖于特定的雷达数据集,不能在其他图像中复制。使用统计方法的另一项应用是基于表面拟合技术,以信息熵作为准则函数,利用参数多项式模型对整幅图像数据进行拟合,然而该方法也是全局性的(Lang 等,2011)。第 3 类方法采用简单的物理模型,基于作为独立变量的入射角 θ_i 来解释特定的角度依赖性。依据 SAR 图像中占主导地位的地物类型,把相应物理模型施加到整幅图像上进行校正。然而,它需要图像中占主导地位的地物类型的先验知识,不能完全补偿图像中其他地物类型的入射角效应(Leclerc 等,2001)。

为此,基于 ENVISAT ASAR 宽模式数据,针对给定的研究区域,假设同一地物类型具有相同的粗糙度、含水量和物理结构,首先利用分水岭分割和区域标记技术实现地物取样,然后使用基本统计量完成地物水平上的入射角效应量化研究;在此基础上,采用结合线性回归估计的余弦朗伯定律,实现对地物后向散射值的按类规格化和辐射校正。

2 研究区域与测试数据

研究区域位于黄渤海地区,包括渤海、山东半岛、辽东半岛、滨海平原和黄海的部分地区(34°N—41°N,115°E—124°E),主要由平原、粉砂淤泥质海岸和近海组成,地势平坦,岸线平直。

其中渤海由渤海海峡、辽东湾、渤海湾、莱州湾和渤海中央盆地 5 个海区构成,由于位于中纬度季风气候区,冬季伴随西伯利亚寒潮入侵渤海地区,每年均有不同程度的结冰现象,初冰期通常为 12 月份,盛冰期为次年的 1 月—2 月,2 月下旬进入融冰期。试验中所用的 7 幅 ASAR 宽观测带模式(WSM)场景均分布在这一时间段中,图像观测带宽度约为 405 km,空间分辨率为 150 m。图 1 给出了其中的 3 幅图像。图 1(a)拍摄于 2005 年 12 月 21 日,距离向向西增加,该时期处于初冰期,沿岸冰刚刚形成;图 1(b)拍摄于 2006 年 2 月 6 日,距离向向东增加,该时期为盛冰期,渤海湾最大浮冰外缘线为 14 n mile,一般冰厚为 5—10 cm,最大冰厚为 25 cm;图 1(c)拍摄于 2006 年 2 月 23 日,距离向向西增加,该时期处于融冰期。3 幅图像中均存在明显的入射角效应,严重阻碍海冰分析人员对海冰的解译,需对这种入射角效应进行补偿。为了保证取样精度,我们还利用了同期冰况图(张启文 等,2006)和光学卫星图像作为辅助信息。

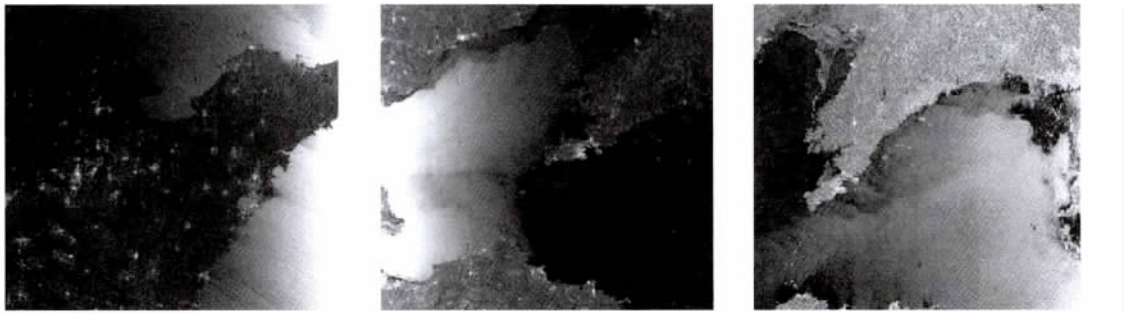

图 1 渤海湾 ASAR 幅度图像

3 绝对定标

虽然未定标的 SAR 图像足以满足定性使用,但定标 SAR 图像对本文的定量研究而言是必不可少的(Johannessen 等,2007)。ASAR WSM 是以地距几何形式发行的卫星图像,图像形成过程中,已对地距图像施加了天线方向图补偿(基于椭圆近似)(Oliver 等,2004)和距离传播损失校正,因此在后续定标过程中无需考虑二者的影响。

针对地距产品,SAR 强度图像的一般形式如式(1)所示。它反映了无噪情形下局部入射角与存储在斜距像元中的 DN 间的关系(Leclerc 等,2001)。

$$\mathrm{DN}^2(i,j) = \frac{K\sigma^0(i,j)}{\sin[\theta_r(i,j)]\cos[\theta_a(i,j)]} \quad \theta_r,\theta_a < 90°$$
$$\mathrm{DN}^2(i,j) = 0 \quad \theta_r \geqslant 90° \qquad (1)$$

式中,K 是绝对定标常数,$\sigma^0(i,j)$ 为第 i 行第 j 列像元的后向散射系数,$\mathrm{DN}^2(i,j)$ 为第 i 行第 j 列像元的强度(DN 正比于后向散射幅度),θ_r 是距离向中的局部入射角,θ_a 为方位向中的局部入射角。式(1)右方分母的含义为地距图像中散射区域的大小是斜

距图像中对应区域的 $[\sin(\theta_r)\cos(\theta_a)]^{-1}$ 倍。

针对 WSM 产品,在参考高程处,假设地形是平坦的($\theta_a = 0$),定标西格玛零定义如下(Rosich 和 Meadows,2004)

$$\sigma^0(i,j) = \frac{\mathrm{DN}^2(i,j)}{K}\sin[\theta_i(i,j)] \quad (2)$$

式中,θ_i 为雷达视线与水平面垂线间的夹角,当地形平坦时,$\theta_i = \theta_r$;所用试验图像的绝对定标常数 K = 7413102.5;入射角的正弦用来补偿地距像元大小的变化,因为在距离向,斜距投影中的分辨单元长度与地距中对应长度间的比例为 $\sin(\theta_r)$,其影响是随着入射角的增加,后向散射值 $\sigma^0(i,j)$ 也随之增大,对入射角效应的补偿效果明显,经过绝对定标后,随着距离向的增大,3 幅 ASAR WSM 图像仍然存在入射角效应。

4 方 法

4.1 取样

为便于对入射角效应进行量化研究与校正,设计了一种独特的同质散射区域取样方法。由于地物种类通常比较复杂且容易混淆,该方法基于空间知识和同质区强度信息对地物进行取样。这里的空间知识主要来自于同一区域的光学图像和同期冰况图,这些辅助空间数据提供了有关地物类型数量的信息,并为雷达强度分析初步定义了取样范围。据此,可把试验图像中的地物种类归类为 3 种类型,即海冰、敞水和陆地。其中海冰主要分布在沿岸区域,即使在盛冰期其在距离向的跨度也较窄;敞水部分在研究时间段内也未见明显的海浪影响;而陆地部分对应山东半岛、辽东半岛和滨海平原的沿海地带。由于整个研究区域地势平坦,我们忽略了地形和局部入射角效应,因此未使用数字高程模型对阴影和叠掩区域进行屏蔽。

地物类型的精确提取必须借助于图像处理中的分割与分类技术。斑点噪声是影响 SAR 图像分类精度的主要障碍,基于强度信息的取样首先应抑制雷达斑点。为此,我们采用分水岭算法(Vincent 和 Soille,1991)将图像分割为众多具有相对一致后向散射值的小区域。假设每个区域 v 由一组属于该区域的像素位置 S_v 构成,S_v 中各位置的强度矢量记为 $\{y_s \mid s \in S_v\}$,那么通过对 v 中所有位置处的强度矢量求平均,即可得到 v 上的特征强度矢量 y_v,从而降低了斑点噪声。接下来,依据地物类型数量这一先验知识,采用基于区域的 K-均值聚类算法(Kanungo 等,2002),为每一分割区域 v 分配最优标记。在该步骤中,并未执行区域合并操作,因而保证了入射角效应的渐变性。这里所采用的分割与分类技术指的是非监督低级分类方法。

入射角的 1°距离槽是雷达散射分析常用的基本单位,每个距离槽代表了 1°入射角对应的观测范围。对地物取样之后,经由 1°距离槽给出平均西格玛值,进而得到从近距到远距的相关地物的西格玛零值的变化曲线。整个取样过程如图 2 所示。

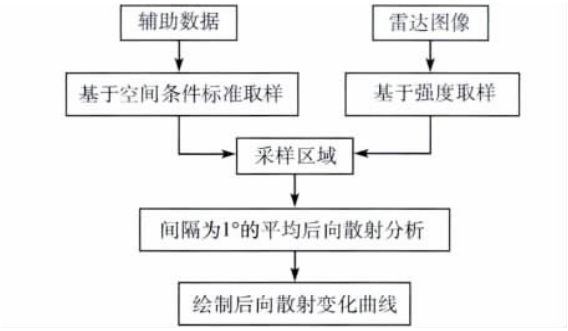

图 2 取样过程

大多数研究中,实地考察通常是学习样本选取的首选。然而,如果实地调查受限或区域访问受当地条件限制(如北极地区),则实现传统的实地验证是不切实际的。而这里提出的基于空间知识和同质区强度信息的地物取样策略,却能产生高效的优化取样结果,表明该策略具有推广应用价值。

4.2 地物水平上的后向散射分析

考虑反射目标,本节针对 ENVISAT ASAR 图像进行基于地物水平上的量化研究,并对雷达后向散射进行分析。

采用图 2 所描述的取样方法,识别海冰、敞水和陆地区域,分别如图 3 的白色、浅灰色、深灰色区域所示,并绘制其经过传统的绝对定标后距离向上的西格玛零值的变化趋势。3 幅图像的海冰分别处于初冰期、盛冰期和融冰期。如图 4 所示,图中均显示了较明显的入射角效应,相对于海冰和陆地,敞水的变化曲线波动最大。3 幅图像的陆地区域沿距离向的后向散射变化趋势大致相同。

如表 1 所示,通过对海冰、敞水和陆地的数据分析可知,经过绝对定标后,随着入射角的变化,海冰、敞水与陆地的后向散射变化各不相同,敞水的辐射变化最大。这些变化是在同种地物类型中观察到的,假设同一地物类型具有相同的粗糙度、含水量和

物理结构,故平均后向反射系数的降低仅归因于入射角和地物类型。由于不同地物类型的后向散射值受入射角的影响不同,因此必须在地物类型的水平上考虑校正方法,而不是整幅图像。

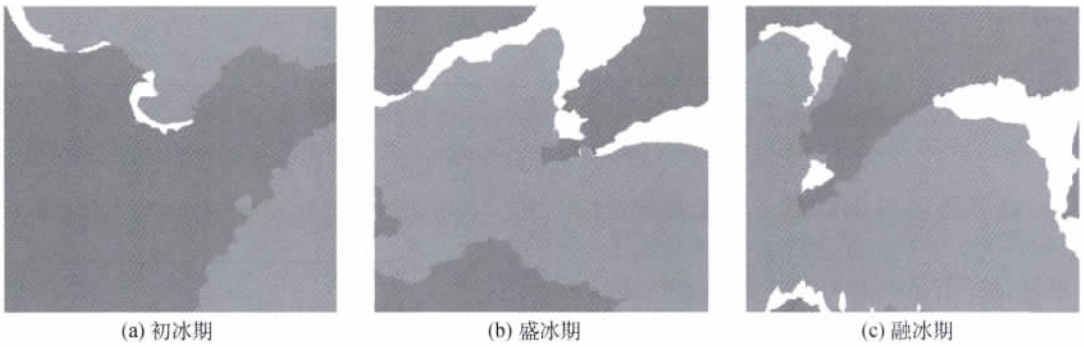

(a) 初冰期 (b) 盛冰期 (c) 融冰期

图 3 取样后的图像

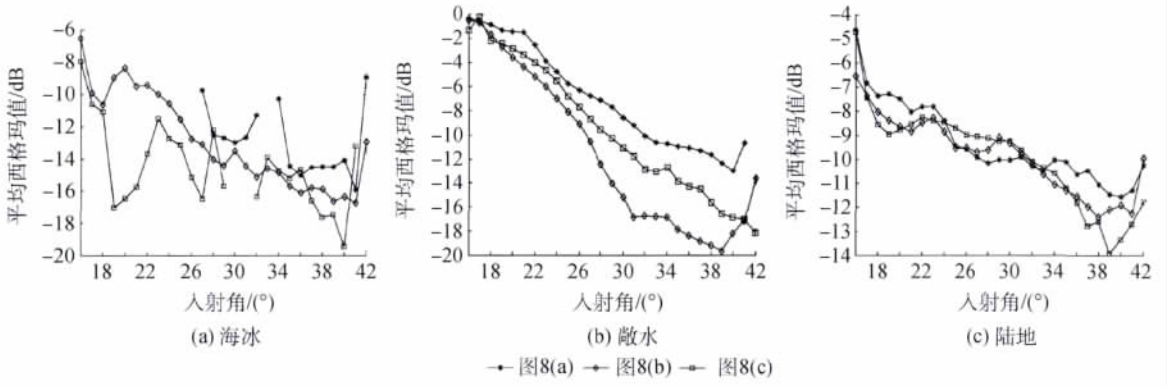

图 4 针对地物类型的后向散射曲线图

表 1 海冰、敞水和陆地的后向散射系数

后向散射/dB	海冰			敞水			陆地		
	最大值	最小值	变化量	最大值	最小值	变化量	最大值	最小值	变化量
图 1(a)	-9.10	-16.11	7.01	-0.02	-13.20	13.18	-5.17	-11.76	6.59
图 1(b)	-7.08	-16.93	9.85	-0.08	-19.86	19.78	-7.10	-12.43	5.39
图 1(c)	-8.52	-19.64	11.12	-0.23	-18.14	17.91	-4.12	-13.92	9.80

4.3 校正方法

针对所研究的各种地物类型,一旦确定并量化了入射角效应,就需要寻找一种沿距离向的辐射度量规格化方法来补偿该效应。

本文提出的校正模型基于辐射传输理论中的朗伯定律(Ulaby 等,1981; Menges 等,2001b)。若散射目标为完美的朗伯散射截面,则辐射波前完全反射回天线,后向散射系数 σ^0 将服从简单的余弦定律

$$\sigma^0 = \sigma_0^0 \cos[\theta_r(i,j)] \cos[\theta_a(i,j)] \quad (3)$$

这里 σ_0^0 是依赖于地物类型的系数。

针对完美的粗糙表面,波前并不完全反射回天线,则后向散射系数服从平方余弦定律

$$\sigma^0 = \sigma_0^0 \cos^2[\theta_r(i,j)] \cos^2[\theta_a(i,j)] \quad (4)$$

若散射目标为分布式独立点散射体,则

$$\sigma^0 = \sigma_0^0 \quad (5)$$

显然,单一模型不可能对图像中呈现的任一地物都适用,而我们希望找出能与各种地物类型相适应的通用后向散射模型,为此,在式(3)—(5)的基础上,设计了一种通用描述

$$\sigma^0 = \sigma_0^0 \{\cos[\theta_r(i,j)] \cos[\theta_a(i,j)]\}^n \quad (6)$$

这里幂指数 n 的取值将不再仅限于 0、1 和 2,因为寻求 n 的较佳估计可以产生更佳的规格化曲线,即沿距离向的规格化曲线具有更好的平坦度。

假设地形是平坦的($\theta_a = 0$),则 $\theta_i = \theta_r$,式(6)可简化为

$$\sigma^0 = \sigma_0^0 \cos^n(\theta_i) \quad (7)$$

为了补偿入射角效应,我们经由线性回归对式(7)中的 n 进行估计

$$y = nx + b \quad (8)$$

式中 $y=\lg(\sigma^0)$,$x=\lg(\cos\theta_i)$,$b=\lg(\sigma_0^0)$ 。

因此,校正模型为

$$\sigma_n^0 = \sigma^0\cos^n(\theta_i) + b \tag{9}$$

这里 σ_n^0 代表校正后的后向散射估计值。

5 实验结果及分析

针对 3 幅 ENVISAT 获取的 ASAR 图像,将后向散射值规格化方法应用到受影响的 3 种类型: 海冰、敞水和陆地。经由线性回归模型式(8)估计校正因子 n 和系数 b,针对上述各个类型的结果如表 2 所示。此外,对海冰、敞水和陆地分别进行后向散射建模,对入射角效应进行校正。用所提出的校正方法开展实验,将按类校正结果与传统的利用绝对定标(式(2))的校正结果和一阶余弦校正(Menges 等,2001a; Ulaby 等,1981)结果相比较,如图5、图 6 和图 7。实验表明本文采用的方法简单,易于实现,耗时短,能有效地对 ENVISAT ASAR 图像的入射角效应进行校正。

从图 5—图 7 的数据变化可以看出,无论是经过绝对定标校正,一阶余弦校正还是按类校正,海冰、敞水和陆地在距离向上的亮度值均得到一定的增强。但是绝对定标和一阶余弦校正针对的均是整幅图像,忽略了地物类型空间分布的影响,虽然图像的入射角效应得到了一定的补偿,但是校正后的图像在远距离处仍然存在残存的入射角效应。

表 2 针对海冰、陆地和敞水的系数 n 和 b 值

图 8	海冰		敞水		陆地	
	n	b	n	b	n	b
(a)	0.81	-1.49	12.04	-0.11	1.85	-1.54
(b)	2.65	-1.75	10.17	-0.64	2.18	-1.36
(c)	1.54	-1.63	10.29	-0.45	2.58	-1.66

本文采用基于地物类型的按类校正方法,校正后海冰、敞水和陆地的后向散射值得到不同程度的补偿。经过按类校正后图像的后向散射相对均匀,消除远距的入射角效应,校正效果更好。总体来说,按类校正后的曲线相对于绝对定标和一阶余弦校正后的曲线,更趋于平滑稳定,校正后图像中的地物类型显得更加清晰。对比图 8、图 9 和图 10,从视觉上来分析校正后的变化,海冰、敞水和陆地经过按类校正后,整体效果优于绝对定标和一阶余弦校正的结果,入射角效应被消除,主要体现在图像中海水的远距离部分,后向散射值得到明显增强。海冰、敞水和陆地的灰度值差距变大,不仅有助于人工判读,也有利于提高高级分类精度。

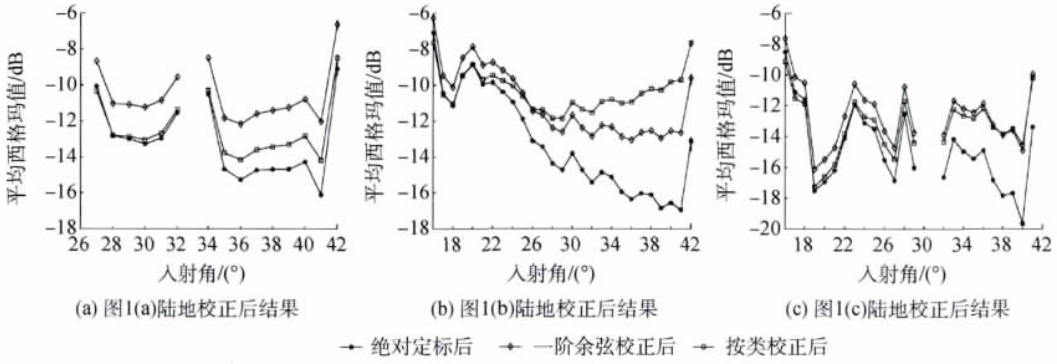

图 5 海冰后向散射估计值随入射角变化曲线对比

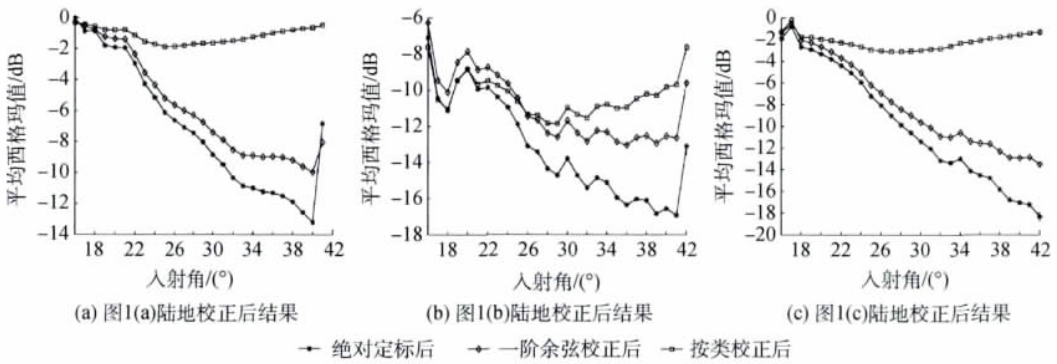

图 6 敞水后向散射估计值随入射角变化曲线对比

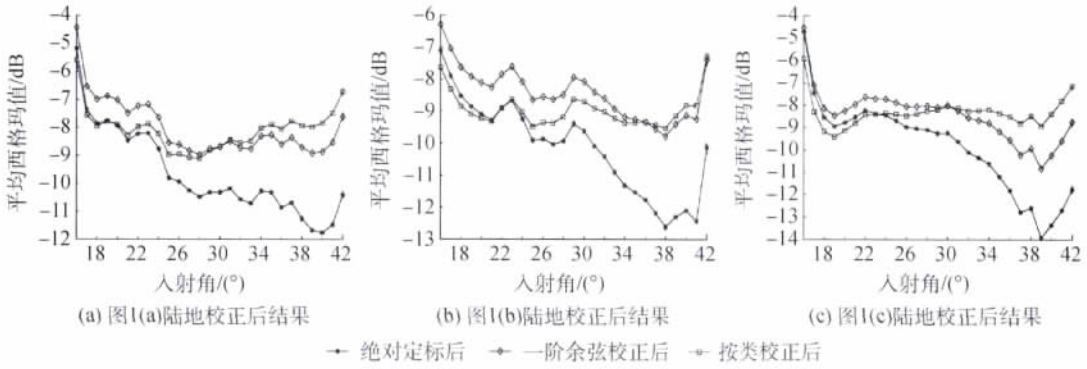

图 7 陆地后向散射估计值随入射角变化曲线对比

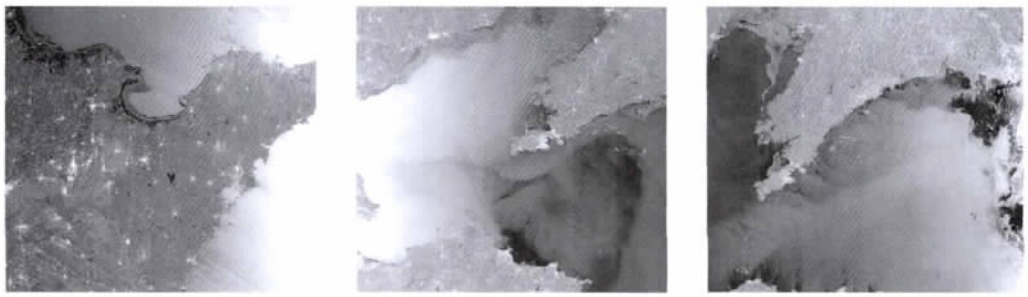

图 8 渤海湾 ASAR 图像经过绝对定标后的结果

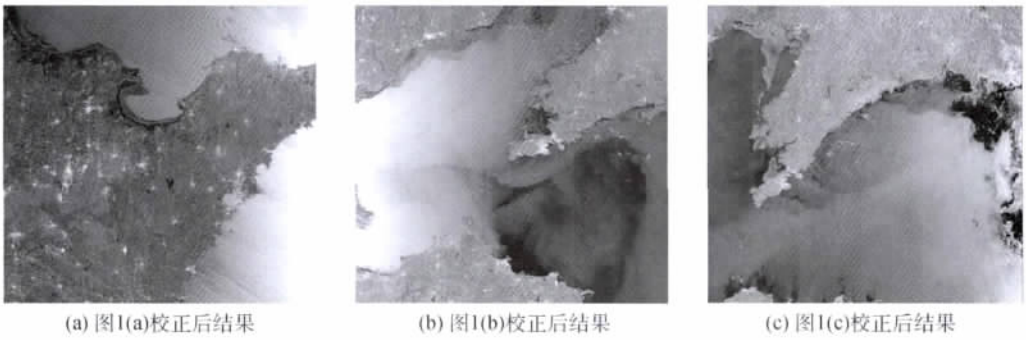

图 9 渤海湾 ASAR 图像经过一阶余弦校正后的结果

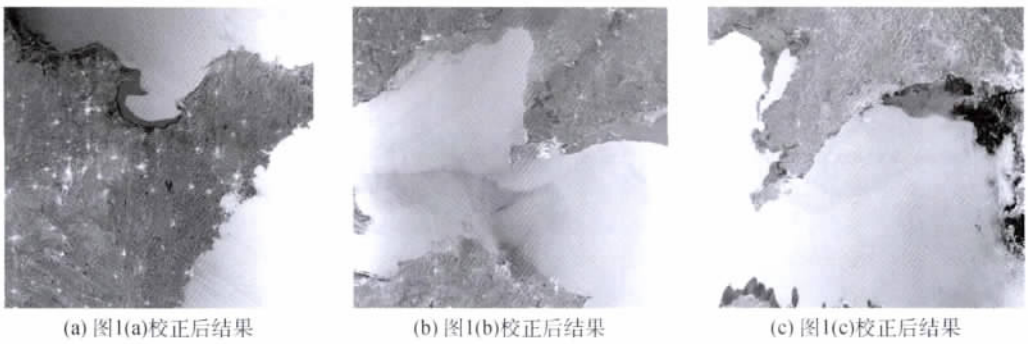

图 10 渤海湾 ASAR 图像经过分类校正后的结果

不同的地物类型,其后向散射值受入射角的影响各不相同,校正因子也不相同。含水量较高的地物类型(如本文中的敞水),其入射角效应大于海冰和陆地,且校正因子最大,经过校正后,敞水的入射角效应明显得到改善。对同种地物类型进行分析,如海冰,尽管海冰在整幅图像中占的比例不大,但也

呈现出一定的入射角效应。通过观察表 2 数据发现,盛冰期中海冰的校正因子最大,初冰期中海冰的校正因子最小。结果表明,针对大多数地物类型,从近距到远距可以检测到后向散射呈现递减趋势。对星载观测来说,这与已有研究建议在校正地形效应之后忽略入射角效应是矛盾的。在处理观测带宽几百公里的星载宽观测带图像时,应该考虑雷达后向散射上的入射角效应。

6 结 论

对多幅 ASAR WSM 图像中的后向散射值的角度变化进行了测量和分析,再次验证了宽观测带模式下的入射角效应不容忽略,特别是海冰和敞水两种类型。并在量化研究的基础上,利用结合线性回归估计的余弦朗伯定律,完成了地物后向散射值的按类辐射校正。与传统的利用绝对定标公式的效果相比,本文方法能更有效地补偿宽观测带 SAR 图像的入射角效应。

大多数卫星 SAR 地面接收站都采用绝对定标公式中的正弦项或一阶余弦校正来抵消距离向后向散射变化,忽视了空间地物类型的变化。但我们认为,对宽观测带星载 SAR 应用而言,应该考虑采用更彻底的校正方案,即考虑地物类型分布的方案。此外,由试验观察可知,校正结果中的估计值 n 和 b,也可用于地物类型的高级分类。

参考文献(References)

Baker J R, Mitchell P L, Cordey R A, Groom G B, Settle J J and Stileman M R. 1994. Relationships between physical characteristics and polarimetric radar backscatter for corsican pine stands in thetford forest, U. K. International Journal of Remote Sensing, 15(14): 2827 – 2849 [DOI: 10.1080/01431169408954287]

Israelsson H, Askne J and Sylvander R. 1994. Potential of SAR for forest bole volume estimation. International Journal of Remote Sensing, 15(14): 2809 – 2826 [DOI: 10.1080/01431169408954286]

Johannessen O M, Alexandrov V Y, Frolov I Y, Sandven S, Pettersson L H, Bobylev L P, Kloster K, Smirnov V G, Mironov Y U and Babich N G. 2007. Remote Sensing of Sea ice in the Northern Sea Route: Studies and Applications. Chichester, UK: Springer

Kanungo T, Mount D M, Netanyahu N S, Piatko C D, Silverman R and Wu A Y. 2002. An efficient K-means clustering algorithm: analysis and implementation. IEEE Transactions on Pattern Analysis and Machine Intelligence, 24(7): 881 – 892 [DOI: 10.1109/TPAMI.2002.1017616]

Lang W H, Wang J S, Yang X Z and Wang G Z. 2011. Multi-exponential model based bias field correction of SAR sea ice image. Journal of Remote Sensing, 15(1): 163 – 172

Leclerc G, Beaulieu N and Bonn F. 2001. A simple method to account for topography in the radiometric correction of radar imagery. International Journal of Remote Sensing, 22(17): 3553 – 3570 [DOI: 10.1080/01431160010007060]

Mäkynen M P, Manninen A T, Similä M H, Karvonen A J and Hallikainen M T. 2002. Incidence angle dependence of the statistical properties of C-Band HH-Polarization backscattering signatures of the Baltic sea ice. IEEE Transactions on Geoscience and Remote Sensing, 40(12): 2593 – 2605 [DOI: 10.1109/TGRS.2002.806991]

Menges C H, Van Zyl J J, Hill G J E and Ahmad W. 2001a. A procedure for the correction of the effect of variation in incidence angle on AIRSAR data. International Journal of Remote Sensing, 22(5): 829 – 841

Menges C H, Hill G J E, Ahmad W and van Zyl J J. 2001b. Incidence angle correction of AirSAR data to facilitate land-cover classification. Photogrammetric Engineering and Remote Sensing, 67(4): 479 – 489

Monsiváis A, Chenerie I, Baup F, Mougin E and Sarabandi K. 2006. A ngular normalization of ENVISAT ASAR data over Sahelian-grassland using a coherent scattering model. Progress in Electromagnetics Research Symposium, 2(1): 94 – 98

Oliver C and Quegan S. 2004. Understanding Synthetic Aperture Radar Images. Raleigh, NC: SciTech Publishing, p197

Rignot E, Way J, Williams C and Viereck L, 1994. Radar estimates of a bove ground biomass in boreal forests of interior Alaska. IEEE Transactions on Geoscience and Remote Sensing, 32(5): 1117 – 1124 [DOI: 10.1109/36.312903]

Rosich B and Meadows P. 2004. Absolute calibration of ASAR Level 1 products generated with PF-ASAR. Issue 1, Revision 5, European Space Agency

Ulaby, F T, Batlivala P P and Dobson M C. 1978. Microwave backscatter dependence on surface roughness, soil moisture, and soil texture: Part I. Bare soil. IEEE Transactions on Geoscience Electronics, GE – 16(1978) 4: 286 – 295

Ulaby F T, Bush T F and Batlivala P P. 1975. Batlivala, Radar response tovegetation II: 8—18 GHz band. IEEE Transactions on Antennas and Propagation, AP – 23(1975) 5: 608 – 618

Ulaby F T, Moore R K and Fung A K. 1981. Microwave Remote Sensing: Active and Passive: Vol. I microwave remote sensing fundamentals and radiometry Vol. II radar remote sensing and surface scattering and emission theory Vol. III from theory to applications. Addison-Wesley, 456

Vincent L and Soille P. 1991. Watersheds in digital spaces: an efficient algorithm based on immersion simulations. IEEE Transactions on Pattern Analysis and Machine Intelligence, 13(6): 583 – 598 [DOI: 10.1109/34.87344]

Yu Q Y. 2006. Automated SAR Sea Ice Interpretation. Canada: University of Waterloo

张启文, 白珊, 李宝辉, 刘煜, 李春花. 2006. 2005—2006 年冬季渤海冰情及海冰警报. 海洋预报, 23(增刊): 17 – 26